minerals

MDPI

Article

SIMS Zircon U-Pb Ages and O Isotope Compositions of Gabbro from the Laguoco Ophiolite from Western Shiquanhe–Yonzhu Suture Zone (Tibet) and Their Geological Significance

Yong Wu [1,*], Ming-Kuan Qin [1], Cai Zhang [2,*], Guo-Lin Guo [3], Dong-Fa Guo [1], Fei Liu [4], Wei-Wei Wu [5] and Jing-Sui Yang [5]

[1] CNNC Key Laboratory of Uranium Resources Exploration and Evaluation Technology, Beijing Research Institute of Uranium Geology, Beijing 100029, China
[2] Shanxi Museum of Geology, Taiyuan 030024, China
[3] Faculty of Earth Science, East China University of Technology, Nanchang 330013, China
[4] CARMA, Key Laboratory of Deep-Earth Dynamics of Ministry of Natural Resources, Institute of Geology, Chinese Academy of Geological Sciences, Beijing 100037, China
[5] School of Earth Sciences and Engineering, Nanjing University, Nanjing 210023, China
* Correspondence: cnncwuyong@outlook.com (Y.W.); 2001130123@email.cugb.edu.cn (C.Z.); Tel.: +86-010-64960551 (Y.W)

Abstract: The Shiquanhe–Laguoco–Yongzhu–Jiali ophiolite mélange belt in Tibet includes the Laguoco Tso ophiolite as part of its western segment. Researchers studying the evolution of the Tibetan Plateau and the Tethys have taken a keen interest in the debated relationship between this ophiolite belt and the Bangong–Nujiang ophiolite belt. However, there is little research in this field. This study reports the rock geochemistry, SIMS (the secondary ion mass spectrometry) zircon U-Pb ages, and O isotope compositions of gabbro from the Laguoco ophiolite. Gabbro has substantial depletion in HFSEs (the high field strength elements) such as Th, Nb, Zr, and Hf, as well as exhibits comparatively high $Mg^{\#}$ (80.6 on average), and low K, N, P, and Ti contents. Therefore, it was possibly formed in an intra oceanic subduction island arc environment originating from ~30% partial melting of the depleted spinel lherzolite. The SIMS zircon U-Pb ages of the gabbro samples are 187 ± 1.2 Ma and 189 ± 2.1 Ma, and the weighted averages of $\delta^{18}O$ are 5.24‰ ± 0.12‰ and 5.34‰ ± 0.13‰, which are close to mantle-derived zircon $\delta^{18}O$ (5.3‰ ± 0.3‰). These results suggest that during the Early Jurassic, the Laguoco ophiolite recorded the intra oceanic subduction of the northern branch of the Neo-Tethys.

Keywords: ophiolite; Laguoco; secondary ion mass spectrometry (SIMS); zircon U-Pb ages; O isotope; Tibet

Citation: Wu, Y.; Qin, M.-K.; Zhang, C.; Guo, G.-L.; Guo, D.-F.; Liu, F.; Wu, W.-W.; Yang, J.-S. SIMS Zircon U-Pb Ages and O Isotope Compositions of Gabbro from the Laguoco Ophiolite from Western Shiquanhe–Yonzhu Suture Zone (Tibet) and Their Geological Significance. *Minerals* **2022**, *12*, 1184. https://doi.org/10.3390/min12101184

Academic Editor: Rubén Díez-Fernández

Received: 31 July 2022
Accepted: 14 September 2022
Published: 21 September 2022

1. Introduction

Ophiolites are commonly thought to be remnants of the paleo-oceanic lithosphere and a crucial rock assemblage among those studying the history of paleo-oceanic tectonics and magmatic evolution [1–3]. As recorders of the formation, convergence, and closure of paleo-oceans that offer critical evidence for studying magmatic evolution and melt–rock reaction in the oceanic lithosphere's upper mantle, they are extensively employed in plate tectonic system investigations [4–6].

The Shiquanhe–Laguoco–Yongzhu–Jiali ophiolite mélange belt (abbreviated as "SLYJZ") in the central Tibetan plateau is located in the northern part of the Yarlung– Zangbo suture zone, near the southern part of the Bangong–Nujiang suture zone (Figure 1) [7,8]. The NWW–EW–SE-trending belt starts from the Shiquanhe River in the west and runs southeastward past Guchang, Laguoco, Asuo, Shenzha, Yongzhu, and Kaimeng, over a distance of more than a thousand kilometers with a width of 3km–35 km [6,9,10]. The ophiolite's petrogenesis in this belt and the associated sedimentary rock formations have been widely investigated since the 1990s [10,11]. Particularly, as geological mapping efforts

of the Tibetan plateau roll out, novel insights into the distribution, rock composition, formation age, and tectonic background of the ophiolite are gained. However, the ophiolite's origin and the tectonic affiliation of this belt remain undetermined, restraining further understanding of critical geological aspects of the Tibetan plateau. The ophiolite's formation environment (intraplate, oceanic island, forearc/back arc basin, or supra subduction zone), subduction polarity (southward or northward), ocean opening mechanism, and opening/closing time (the oceanic crust began to form in the Late Triassic, subducted in the Early to Middle Jurassic; the oceanic basin remained open until the Early Cretaceous) remains debatable [9,12–19]. Thus, more work is required to define the precise tectonic evolution of the SLYJZ suture zone.

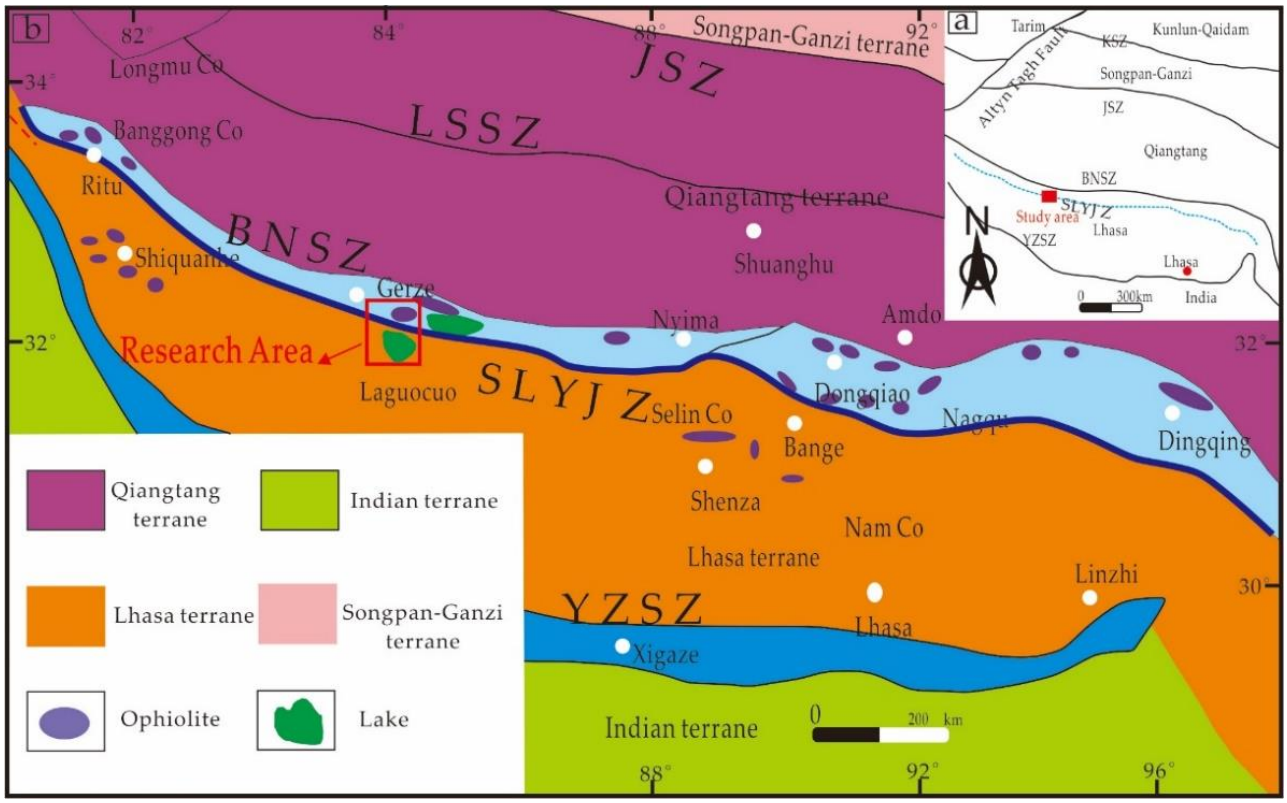

Figure 1. (**a**) The main geotectonic units of eastern Asia. (**b**) The simplified geotectonic map of the Tibetan Plateau from the Shiquanhe–Laguoco–Yongzhu–Jiali zone was modified after [12]. KSZ: the Kunlun–Qaidam suture zone, JSZ: the Jinsha suture zone, LSSZ: the Longmuco–Shuanghu suture zone, BNSZ: the Bangong–Nujiang suture zone, YZSZ: the Yarlung–Zangbo suture zone.

Fan Shuaquan et al. [20] argued that the SLYJZ suture zone formed in a supra subduction zone tectonic environment and is an SSZ-type (the supra subduction zone) ophiolite. Previous investigations have dated the Laguoco Tso ophiolite to the Jurassic–Early Cretaceous on the following basis: (1) Regarding the age of the Laguoco Tso ophiolite, the disagreement relates to whether it originated in the Middle Jurassic or Early Cretaceous. For gabbro in the Laguoco Tso ophiolite, the Ar-Ar age is 125 Ma; further, the zircon ages are 155.3 ± 2.6 Ma and 166.6 ± 2.5 Ma, whereas the zircon ages for plagiogranite in the related ophiolite are 155.3 ± 2.6 Ma, 166.6 ± 2.5 Ma, and 190 Ma [14,21–23], showing that the Laguoco Tso oceanic basin was primarily formed in the Middle Jurassic. (2) Regarding the Laguoco Tso ophiolite's highly controversial tectonic background, Wang Baodi et al. [22] propose that it was produced in an inter arc basin. Regarding its tectonic background, opinions include a back arc basin, a mid-oceanic ridge, and intra oceanic subduction. Therefore, probing deeper into the Laguoco Tso ophiolite is crucial for debates over the Laguoco Tso ophiolite's tectonic evolution in the SLYJZ suture zone.

Based on past findings and field activities, this study comprises comprehensive petrological, geochemical, and chronological research on gabbro, incorporating zircon O isotope analysis to allow further examination of the petrogenesis. In addition, evolutionary history of the ophiolite as well as valuable information for a better understanding of regional tectonics and evolution are provided.

2. Geological Overview and Geological Characteristics of Laguoco Ophiolite

The study area is located at the central Tibetan Plateau, about 30 km south of Gerze county, tectonically along the north bank of the Laguoco ophiolite on the southern boundary of the western SLYJZ suture zone (Figure 2). It occurs E-W in an irregular lenticular form, extending ~30 km by 3–5 km width, with an exposed area of ~120 km^2, connected to the Guchang ophiolite mélange belt to the west. The Laguoco Tso ophiolite is on the north bank of Laguoco Lake, where plate tectonic processes have dismembered the rock body. The Laguoco Tso ophiolite is in fault contact with the Lower Cretaceous Langshan formation (K_1l) marine limestone as structural emplacements. The Early Permian Lower Xiala formation (P_1x), whose dominant lithology is grayish white dolomite and purplish red bioclastic limestone, is in contact with the south side. It is in fault contact with Late Jurassic to the Early Cretaceous Zelong group (J_3K_1z) volcanic rocks, whose lithologies are mainly composed of particolored sandstone, andesitic volcanic breccia, rhyolitic dacite, and a lesser amount of microcrystal limestone. The north side of the area is bounded using dextral strike-slip structures with the fault plane dipping 45°–60° N. The ophiolite is overthrust by the Late Carboniferous to Early Permian Laga formation (C_2P_1l) within the belt, which comprises grayish green quartz sandstone, gravelly sandstone, siltstone, and shale. Early Cretaceous Duoni formation (K_1d) volcanic rocks comprise a series of sporadically distributed, intermediate acidic volcanic rocks, mainly andesite and rhyolite (Figure 2).

According to a geological field survey, the Laguoco Tso ophiolite is severely fractured through tectonic processes. With Early Cretaceous (K_1l) limestone blocks present in the basic rocks, the ophiolite has almost all compositional units, such as mantle peridotite, cumulate, pillow lava, diabase, plagiogranite, and silicalite. Primary rocks in the mantle peridotite include serpentinite, dunnite, lherzolite, and harzburgite, most of which have been intensely serpentinite. The rocks commonly feature a reticular texture and a massive structure.

Cumulates are sporadically seen and frequently overburdened by Quaternary in the study area. The cumulate is mainly a series of cumulate gabbro comprised of homogeneous gabbro and a lesser amount of stratiform gabbro. The latter has a typical cumulate texture including various types of rhythmic layers commonly 1 cm–2 cm thick with quasi-stratification. The former features a massive structure. The pillow basalt is primarily discovered on the Laguoco Tso Lake's north bank, showing a typical pillow structure. Therefore, the pillow basalt is commonly quite fractured in late tectonic processes, but the pillow shape is still discernible. These grayish green rocks feature porphyritic texture and pillow structure. The phenocryst mainly comprises plagioclase. Many of the rocks contain pore structures that are irregularly shaped and filled with late calcite, chlorite, quartz, and other minerals. The diabase dykes differ in width, commonly between 10 cm and 15 cm, and stretch 50 m to 200 m in length. Mostly these typically grayish green rocks feature grayish green texture and massive structure. Mostly plagiogranite exists in basic rocks as irregular gray dykes. Generally, the dykes are 3 cm–60 cm across, lying in intrusive contact with the surrounding rock, and feature granular texture and massive structure. Several of the dykes have been chloritized to differing degrees in later years. The silicalite is mainly purplish red. Most of these rocks feature a cryptocrystalline texture and massive structure. They lie primarily in structural contact with basic rocks and are widely distributed in the study area (Figure 3a–f).

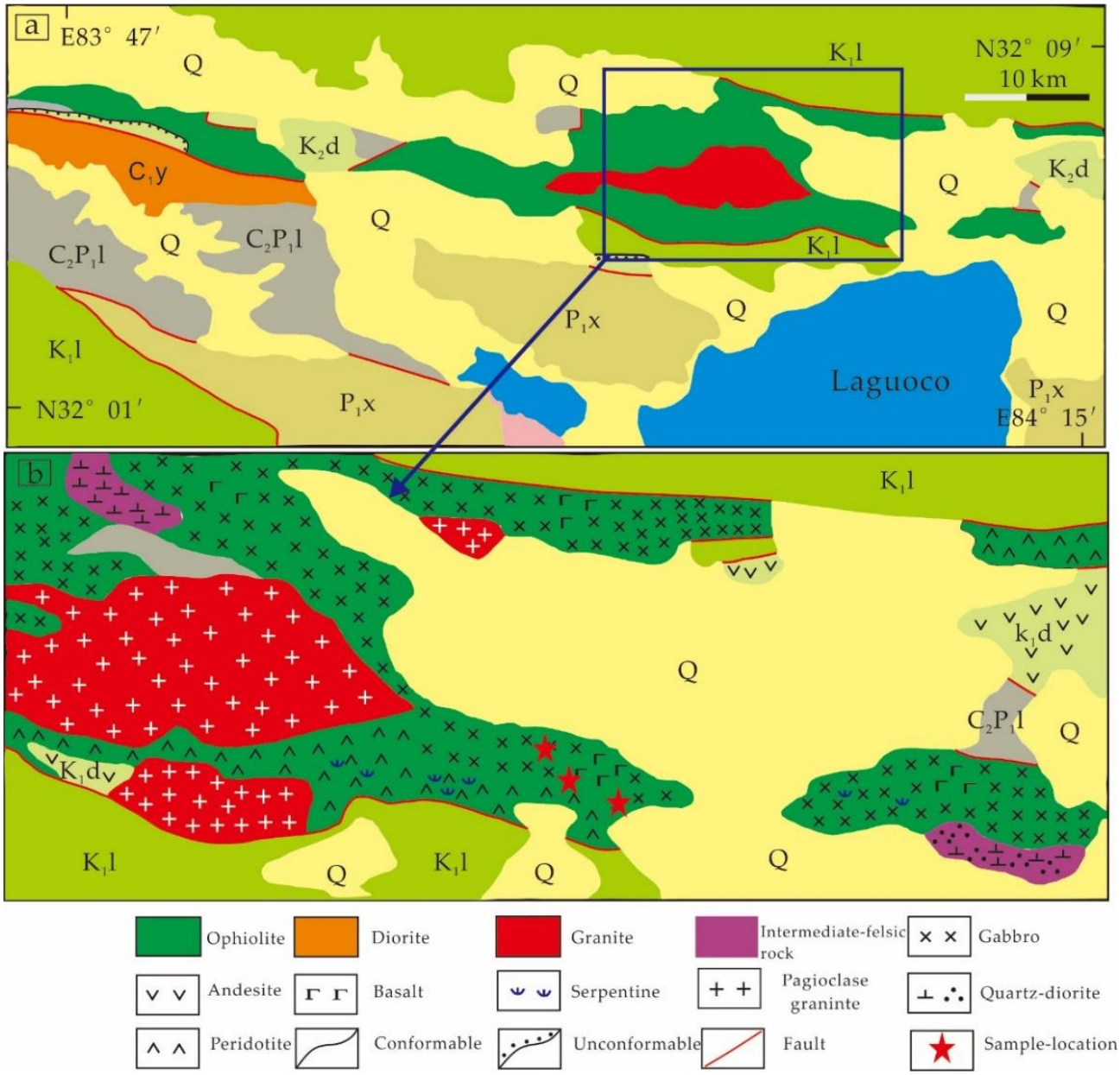

Figure 2. (**a**) Main geotectonic units of Laguoco. (**b**) Simplified geologic map of the Laguoco ophiolite, modified after [12]. C_1y: Early Carboniferous Yongzhu formation; C_2P_1l: Late Carboniferous–Early Permian Laga Formation; P_1x: Early Permian Xiala Formation; K_1l: Early Cretaceous Lanon Formation; K_1d: Early Cretaceous Duoni Formation; Q: Quaternary.

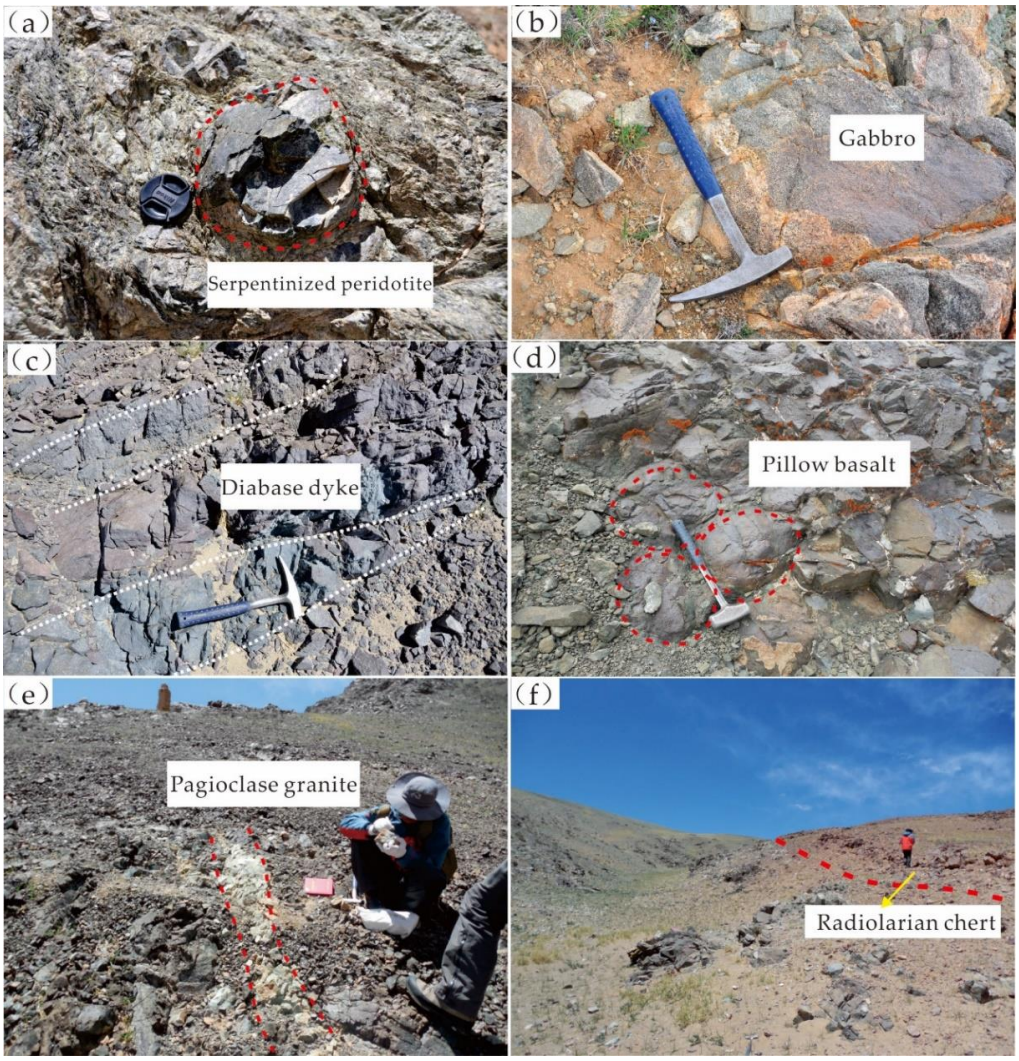

Figure 3. (a–f) Field photographs of the Laguoco ophiolite. (**a**) Serpentinzed peridotite; (**b**) Isotropic gabbro; (**c**) Diabase dyke; (**d**) Pillow basalt;(**e**) Plagioclase granite; (**f**) Overlying radiolarian chert from Laguoco.

3. Analytical Methods

3.1. Petrographic Analysis

The most abundant rocks in the Laguoco Tso ophiolite are gabbro. Under both field and microscopic analysis, the cumulate gabbro among them appears to be cumulated. These grayish green rocks (Figure 4) feature intermediate fine-grained texture and massive structure. The minerals are mainly plagioclase, pyroxene, amphibole, and low amounts of olivine and chromite. The plagioclase occurs as idiomorphic and hypidiomorphic long columns with a grain size of 0.02 mm–0.05 mm. The rocks are partially chloritized or epidotized. Pyroxene occurs as hypidiomorphic or xenomorphic grains with a grain size of 0.02 mm–0.05 mm.

3.2. Whole-Rock Major and Trace Element Geochemistry

Seven gabbro samples were analyzed for major and trace elements at the National Research Center for Geo-analysis in Beijing, China. Samples were trimmed to remove the oxidized surfaces, cleaned in deionized water, and were then crushed and powered to about 200 meshes within agate mills. Major elements were analyzed by X-ray fluorescence (XRF) spectrometry, with an analytical accuracy of ~1% relative to SiO_2 and 2% relative to the other oxides. The major method and procedure of analysis are described by Chen et al. [24].

Trace elements, including rare elements (REE), were determined by inductively coupled mass spectrometry (ICP-MS). Analytical uncertainties were estimated to be 10% for trace elements with abundances < 10ppm. The detailed methods and procedures are described by Qi and Grégoire et al. [25]. Loss on ignition (LOI) values were determined by gravimetric techniques in which the sample was heated in a closed container and the water vapor was collected in a separate tube, condensed, and then weighed. The detection limit for H_2O and CO_2 was 0.01 wt %. The major and trace element compositions are given in the Table 1.

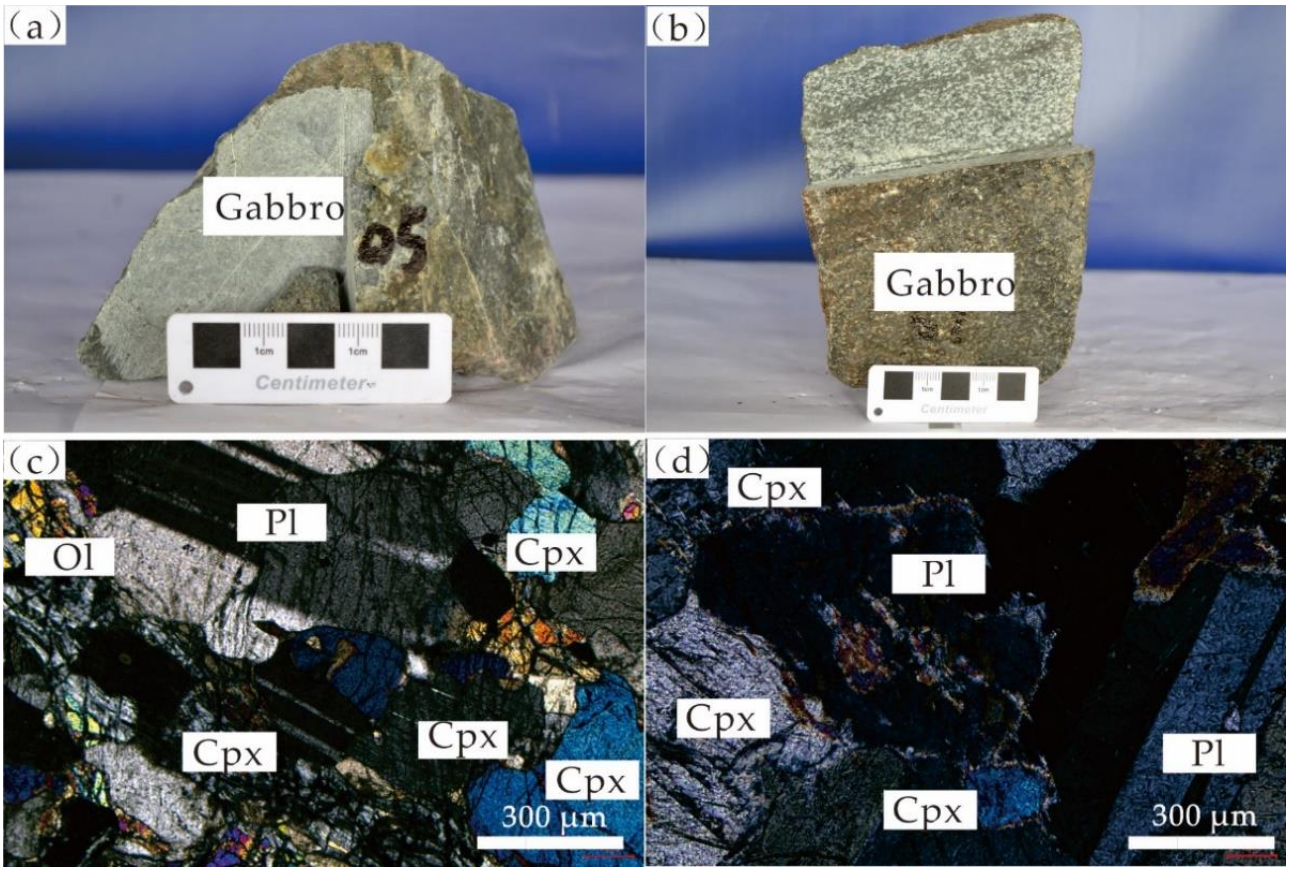

Figure 4. Photomicrographs of the Laguoco Gabbro. (**a**,**b**) The gabbro hand specimen; (**c**,**d**) Isotropic gabbro with gabbro and ophitic textures. Cpx: clinopyroxene; Ol: olivine; and Pl: plagioclase.

3.3. SIMS zircon U-Pb Chronological Test Method

For zircon U-Pb age and O isotopes, two samples from the Laguoco Tso ophiolite (LGC04 and LGC07) were examined using SIMS. Zircon were separated using conventional gravity and magnet separation. With standard zircon Plésovice [26], the sorted zircon grains were pasted on an epoxy resin target together with Qinghu [27], then ground and polished until the zircon core was exposed. Zircon samples were subjected to transmission and reflection photomicrography, cathodoluminescence image analysis, and the zircon target preparation to confirm the morphology and internal texture of zircon and determine the most suitable test area. Finally, the sample target was gold plated in a vacuum to a thickness of ~30 nm.

Table 1. Whole-rock analyses of major (%) and trace element (ppm) of gabbro, Laguoco, Tibet.

Sample	15LGC03	15LGC04	15LGC06	15LGC07	15LGC08	15LGC09	15LGC10
Lithology				**Isotropic Gabbro**			
SiO_2	50.90	51.06	50.85	50.58	49.57	50.45	50.91
K_2O	0.08	0.07	0.13	0.07	0.07	0.06	0.26
Na_2O	1.13	0.83	0.90	0.75	0.90	1.08	1.18
Al_2O_3	15.51	13.26	13.90	13.50	16.74	15.62	15.12
CaO	14.38	14.32	15.16	14.74	17.00	15.84	13.03
Fe_2O_3	1.59	1.67	1.35	1.71	1.34	1.11	1.47
FeO	4.31	4.41	4.32	4.35	3.15	3.70	4.69
MgO	11.77	14.10	13.10	14.02	10.98	11.88	13.03
MnO	0.12	0.12	0.12	0.12	0.10	0.11	0.13
P_2O_5	0.01	0.01	0.01	0.01	0.01	0.01	0.01
TiO_2	0.18	0.16	0.16	0.15	0.15	0.15	0.17
$Mg^{\#}$	78.50	80.96	80.85	80.91	81.79	81.86	79.42
LOI	1.25	1.45	1.68	1.31	1.87	1.56	1.76
Total	100.00	100.00	100.00	100.00	100.00	100.00	99.99
La	0.23	0.14	0.13	0.16	0.18	0.38	0.13
Ce	0.54	0.36	0.36	0.38	0.47	0.71	0.34
Pr	0.11	0.09	0.07	0.08	0.1	0.12	0.08
Nd	1.03	0.72	0.75	0.72	1	1.07	0.72
Sm	0.29	0.23	0.23	0.22	0.3	0.32	0.24
Eu	0.19	0.11	0.13	0.11	0.18	0.18	0.13
Gd	0.52	0.39	0.39	0.4	0.48	0.49	0.39
Tb	0.09	0.07	0.08	0.07	0.08	0.1	0.07
Dy	0.68	0.49	0.56	0.49	0.58	0.61	0.51
Ho	0.15	0.11	0.12	0.11	0.13	0.13	0.11
Er	0.42	0.33	0.36	0.32	0.36	0.37	0.34
Tm	0.06	0.06	0.05	0.05	0.05	0.05	0.06
Yb	0.44	0.32	0.37	0.31	0.36	0.38	0.37
Lu	0.07	0.06	0.06	0.07	0.05	0.05	0.05
Y	4.05	3.15	3.31	2.94	3.56	3.54	3.2
ΣREE	4.82	3.48	3.66	3.49	4.32	4.96	3.54
LREE	2.39	1.65	1.67	1.67	2.23	2.78	1.64
HREE	2.43	1.83	1.99	1.82	2.09	2.18	1.9
LREE/HREE	0.98	0.90	0.84	0.92	1.07	1.28	0.86
$(La/Yb)_N$	0.37	0.31	0.25	0.37	0.36	0.72	0.25
δ Eu	1.50	1.12	1.33	1.13	1.45	1.39	1.30
δ Ce	0.83	0.79	0.93	0.82	0.86	0.82	0.82
Ni	204.00	237.00	174.00	232.00	148.00	147.00	173.00
Zn	36.70	35.90	28.70	28.70	23.20	25.70	32.90
Rb	2.05	0.95	3.51	0.90	1.07	0.65	8.69
Sr	141.00	126.00	161.00	120.00	155.00	149.00	156.00
Cd	0.06	0.07	0.06	0.07	0.07	0.06	<0.05
Cs	10.50	2.43	3.36	1.96	2.34	1.17	5.95
Ba	7.40	10.20	9.58	10.40	9.26	5.31	17.30
Pb	0.45	0.30	0.46	1.09	0.45	0.62	1.25
Th	<0.05	<0.05	<0.05	<0.05	<0.05	<0.05	<0.05
U	0.06	<0.05	0.07	<0.05	<0.05	0.06	<0.05
Nb	<0.05	0.06	<0.05	0.07	<0.05	0.06	<0.05
Ta	<0.05	<0.05	<0.05	<0.05	<0.05	<0.05	<0.05
Zr	1.40	1.22	1.00	1.03	1.42	1.78	0.81
Hf	0.09	0.07	0.07	0.06	0.08	0.10	0.06
Sn	0.07	0.06	0.06	0.14	0.07	0.07	0.05
Ti	1029.00	868.00	830.00	830.00	799.00	795.00	888.00
As	2.93	1.75	5.40	3.44	1.58	2.18	1.11
V	170.00	170.00	164.00	156.00	152.00	142.00	161.00
Sc	55.20	60.80	58.80	54.40	51.30	48.40	53.90

$Mg^{\#}$ = Mg/(Mg + Fe) × 100; LOI: loss on ignition.

SIMS zircon U-Pb age analysis was conducted at the Beijing Research Institute of Uranium Geology using a CAMECA 1280 HR SIMS. The analysis method was the same as that described by Li et al. [28]. Standard zircons and the zircon samples were measured alternately in a ratio of 1:4. The following instrument working parameters were employed: the main ion optical path system was the Kohler model; the main ion beam intensity was ~10nA; the primary mass filter aperture size was 200 μm; the main ion optical path system was modulated, so that the main ion beam spot reaching the sample surface was sized ~20 μm × 30 μm. The secondary ion optical path contrast aperture was 400 μm; the entrance slit was 80 μm; the field aperture was 7000 μm; the energy slit was 50 eV; the exit slit was 173 μm; and the instrument mass resolution was ~7007 (defined by 50% peak height). Secondary ion signals were received using the electron multiplier of a monocollector system. The following signals were sequentially collected: 196 ($^{90}Zr_2{}^{16}O$), 200 ($^{92}Zr_2{}^{16}O$), 200.5, 204 ($^{94}Zr_2{}^{16}O$), 204 (^{204}Pb), 206 (^{206}Pb), 207 (^{207}Pb), 208 (^{208}Pb), 209 ($^{177}Hf^{16}O_2$), ^{232}Th, ^{238}U, $^{232}Th^{16}O$, $^{238}U^{16}O$, and $^{238}U^{16}O_2$. The waiting time before signal collection was: 2.96 s, 0.80 s, 0.80 s, 0.80 s, 1.52 s, 0.80 s, 0.80 s, 0.80 s, 0.80 s, 1.20 s, 0.88 s, 0.88 s, 0.88 s, and 1.04 s. The signal collection time was: 1.04 s, 0.48 s, 4.00 s, 0.64 s, 6.08 s, 4.00 s, 6.00 s, 2.00 s, 1.04 s, 2.00 s, 2.00 s, 2.00 s, 2.00 s, and 2.00 s, respectively. Signals were collected for seven cycles, and the test lasted for ~12 min at each test point. The U-Th-Pb isotope ratios were obtained via correction against standard Plésovice (337 Ma, [26]). Correction against the standard zircon 91500 produced U contents (81 × 10^{-6}, [26]). Single point sample errors were obtained through the standard deviation's joint transmission, obtained by long-term standard sample monitoring (1SD = 1.5%, [28]) and the single point test's internal accuracy; as an unknown sample, data accuracy was monitored against standard sample Qinghu (159.5 Ma, [27]). The measured ^{204}Pb was employed for correcting ordinary Pb. The absolute majority of the ordinary Pb content measured was very low (10^{-6}). Thus, the Pb content was corrected against the mean Pb composition of modern crust as the ordinary Pb composition, assuming that ordinary Pb primarily originates from the surface Pb contaminants brought in during sample preparation. The zircon age standard of Qinghu was used for calibration of Pb/U fractionation and monitoring the quality of unknown dating results. The data were calculated by Isoplot 4.15 [29].

3.4. SIMS Zircon O Isotope Test Method

Zircon O isotope analysis was conducted at the Beijing Research Institute of Uranium Geology using a CAMECA 1280 SIMS. The following test conditions were employed. The primary ion optical path system was a Gaussian model; the main ion aperture was sized 400 μm; the Cs^+ main ion beam intensity was~2nA; the grid scan size was 20 μm; and the main ion optical path system was modulated so that the main ion beam spot reaching the sample surface was sized ~20 μm. Electrons obtained through a vertical-incidence electron gun were evenly applied within 100 μm to neutralize the charge effect of the sample surface. Secondary ions were accelerated through −10 kV voltage; the secondary ion optical path contrast aperture was 400 μm; the entrance slit was 150 μm; the field aperture was 5001 μm; the energy slit was 50 eV; the exit slit was 400 μm; and the instrument mass resolution was about 2400 (defined by 10% peak height). O isotopes were evaluated using a multi-collector. Nuclear magnetic resonance was used to stabilize the field strength. The primary standard sample for the O isotope test was the reference material Penglai zircon ($\delta^{18}O$ = 5.31‰ ± 0.10‰), whereas the quality control standard sample was Qinghu zircon. Secondary ion signals were received through a fixed field using the multi-collector system's Faraday cup. The ^{16}O and ^{18}O signals were collected. The signals were collected for 20 cycles, and the test lasted for ~4 min, including 60 s for pre-denudation and 2 min 40 s for signal collection and instrument parameter optimization at each test point. The single-point test's internal precision was better than 0.2‰ (1σ). SIMS instrument mass fractionation (IMF) was corrected against the Penglai zircon standard. Measured $^{18}O/^{16}O$ ratios were corrected against the Vienna standard mean ocean water (V-SMOW) value

($^{18}O/^{16}O$ = 0.0020052), minus the IMF, and selected as the $\delta^{18}O$ of that point. The following was used:

$$(\delta^{18}O)_M = (((^{18}O/^{16}O)_M/0.0020052 - 1) \times 1000(‰)$$

$$IMF = (\delta^{18}O)_{M(Standard)} - (\delta^{18}O)_{V\text{-}SMOW}$$

$$(\delta^{18}O)_{Sample} = (\delta^{18}O)_M - IMF$$

4. Test Results

4.1. Geochemical Compositions

Table 1 shows the major and trace element analysis findings of gabbro in the research area. The major elements of gabbro were discovered to contain the following: moderate SiO_2 (49.57%–51.06%) content; relatively high MgO (10.98%–14.09%) and CaO (0.92%–1.09%) contents; high $Mg^{\#}$ (78.49%–81.79%); moderate Al_2O_3 (13.26%–16.73%); and low TiO_2 (0.15%–0.18%), Fe_2O_3 (1.34%–1.71%), Na_2O (0.74%–1.13%), K_2O (0.06%–0.13%), and P_2O_5 (0.005%–0.007%) contents. The gabbro samples fall in the basalt region in the TAS (the total alkali silica) discrimination diagram; all samples belong to the low potassium tholeiitic basalt series in the rock series discrimination diagram (Figure 5a,b). The gabbro samples have low contents of REEs(the rare earth elements). With an average of 3.86×10^{-6}, the total REE content varies between 3.48×10^{-6} and 4.82×10^{-6}. All samples appear to be flat in the chondrite-normalized REE pattern (Figure 6a), which indicates slight LREE (the light rare earth elements) depletion, with $(La/Yb)_N$ between 0.84 and 1.07, and an Eu-positive anomaly (Eu/Eu*) between 1.12 and 1.49 with an average value of 1.30. Although it is almost parallel to the N-MORB (the normal middle ocean ridge basalt) curve, its content is substantially depleted relative to N-MORB. In the primitive mantle-normalized trace element pattern (Figure 6b), gabbro is enriched with LILEs(the large ion lithophile elements) such as Rb, Ba, and Sr but depleted in HFSEs such as Th, U, Nb, and Ta, resembling the qualities of island arc basalt.

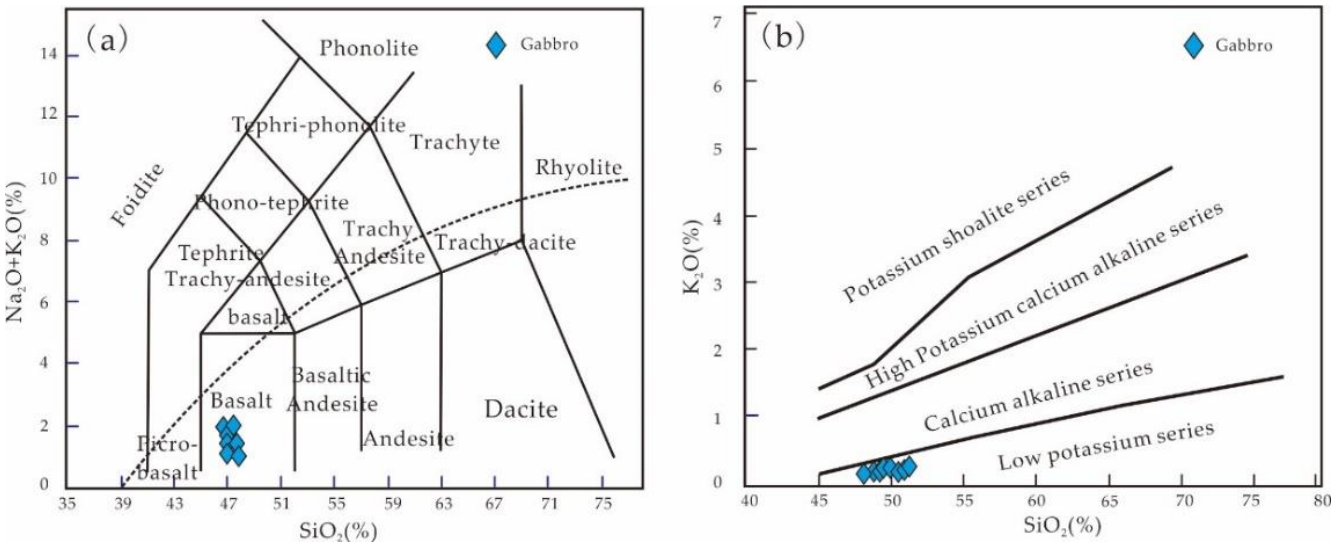

Figure 5. TAS discrimination diagram and rock series of gabbro, Laguoco, Tibet: (**a**) TAS discrimination diagram of samples modified after [30]; (**b**) discrimination diagram of rock series modified after [31].

The gabbro samples generally exhibit an Eu-positive anomaly and similar REE distribution patterns, indicating that they have the same petrogenesis. In addition, the primitive mantle-normalized trace element pattern demonstrates very similar distribution curves: enrichment of LILEs such as Tb, Ba, and Sr, extreme depletion of HFSEs such as Th, U, Nb, and Ta, and substantial depletion of Zr, Ti, and Nb relative to E-MORB(the enrich middle

ocean ridge basalt), possibly an indication of subduction processes [32]. These geochemical characteristics show that the Laguoco Tso ophiolite samples have the characteristics of an SSZ-type ophiolite.

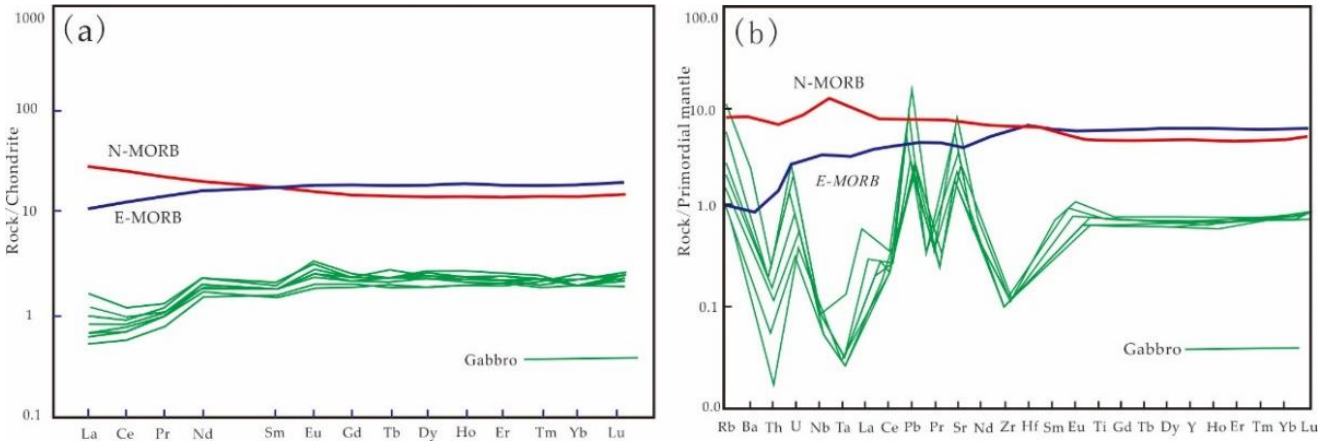

Figure 6. (**a**,**b**) Chondrite-normalized REE and primitive mantle-normalized trace element distribution patterns for gabbro, Laguoco, Tibet, modified after [33].

4.2. SIMS Zircon U-Pb Dating Results

The zircon grains of gabbro samples LGC04 and LGC07 are mostly 100–150 μm in diameter (Figure 7b,d). A few fissures and inclusions can be seen inside the zircons, which are primarily found as long columns or grains with an aspect ratio of 1~2. CL photographs show magmatic oscillatory zoning in zircons, proposing a magmatic origin [33,34].

Studies have shown that magmatic zircons have large Th/U ratios (generally > 0.4), and, for zircons, Th is directly proportional to U [34,35]. From Table 2, for the 23 test points of sample LGC04, the U content is 369–2093 μg/g; the Th content is 174–792 μg/g; and the Th/U ratio is 0.5–1.4. Th and U values were consistent, indicating a magmatic origin. For the 23 test points of sample LGC04, the zircon Concordia age is 189 ± 2.1 Ma (Figure 7a), denoting the crystallization age of the gabbro. For the 12 test points of sample LGC07, the U content is 365–2285 μg/g; the Th content is 207–2044 μg/g; and the Th/U ratio is 0.4–1.2. Th and U are consistent, indicating a magmatic origin. For the 12 test points of sample LGC07, the zircon Concordia age is 187 ± 1.2 Ma (Figure 7c), denoting the crystallization age of the gabbro.

4.3. SIMS Zircon O Isotope Results

Gabbro samples LGC04 and LGC07 from the Laguoco Tso ophiolite were examined using SIMS for zircon O isotopes that were evaluated at the same location as the U-Pb test points. Table 3 lists the test findings.

For zircons of gabbro sample LGC04, the $\delta^{18}O$ is 2.89‰–6.73‰. Except for test point 2, which has a comparatively high $\delta^{18}O$ of 6.73‰, the weighted average of the remaining points is 5.24‰ ± 0.12‰ (Figure 8a), which is the same as mantle $\delta^{18}O$ (5.3‰ ± 0.3‰, [34,35]). For zircons of diabase sample LGC07, the $\delta^{18}O$ is 5.15‰–5.48‰. The weighted average of all points is 5.34‰ ± 0.12‰ (Figure 8b), which is the same as mantle $\delta^{18}O$ (5.3‰ ± 0.3‰, [36]), proposing that this group of zircons originates from mantle-derived crystallization.

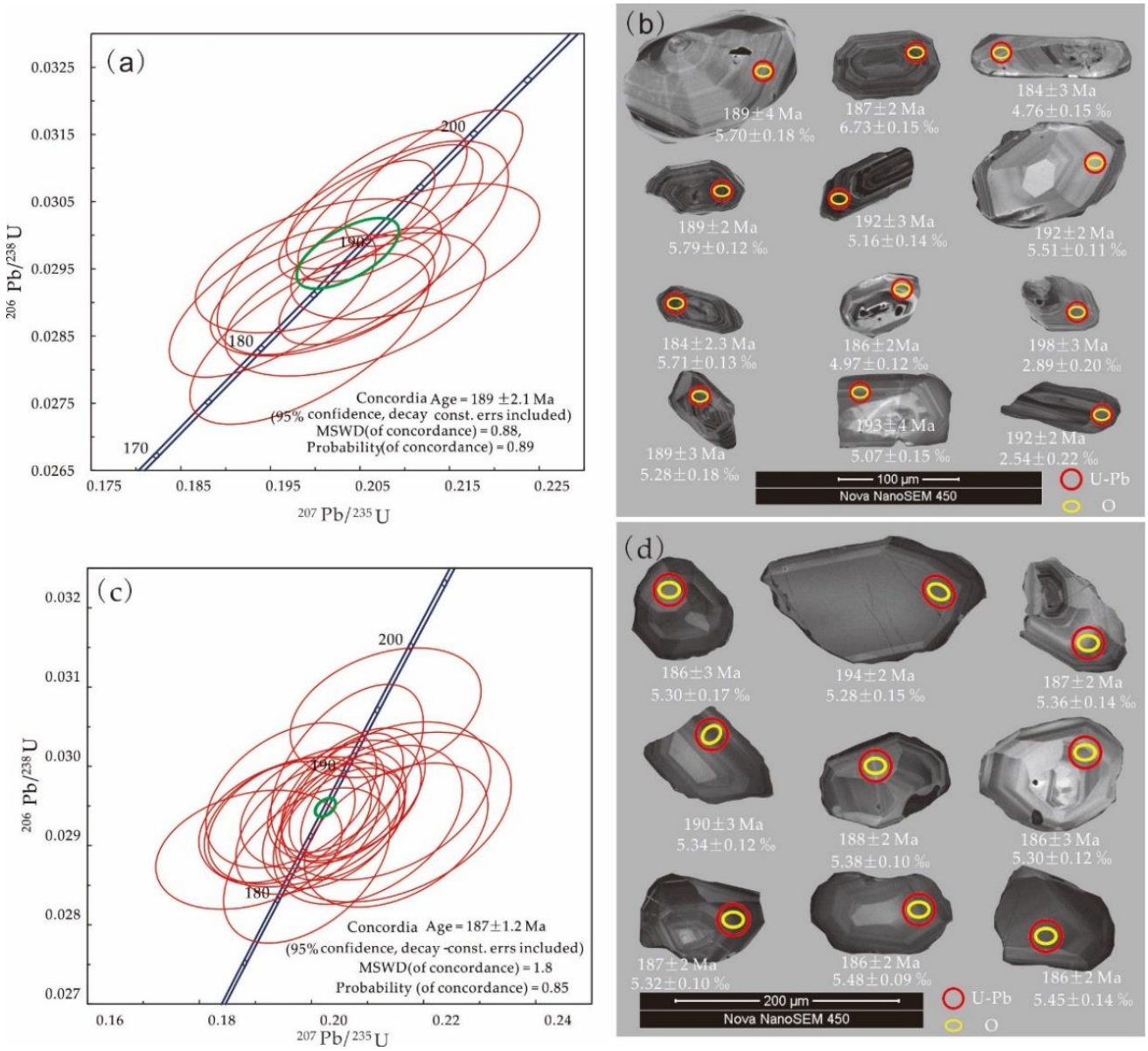

Figure 7. Representative cathodoluminescence (CL) images (**b**,**d**) and Concordia diagrams (**a**,**c**) of zircons in the Laguoco gabbro. Red and yellow circles show the locations of U-Pb dating and O isotope analyses with SIMS, respectively.

Table 2. SIMS zircon U-Pb data of gabbro, Laguoco, Tibet.

Point Number	Isotope Ratio after ^{204}Pb Correction					Isotopic Age (Ma)				Content		
	^{207}Pb/^{235}U	±σ	^{206}Pb/^{238}U	±σ	ρ	^{207}Pb/^{235}U	±σ	^{206}Pb/^{238}U	±σ	U	Th	Th/U
LGC04 Gabbro												
1	0.20532	3.23	0.0298	2.18	0.67503	189.6	5.6	189.4	4.1	480	207	0.432
2	0.20551	1.90	0.0292	1.22	0.64194	189.8	3.3	185.8	2.2	1123	813	0.724
3	0.19938	2.74	0.0285	1.82	0.66531	184.6	4.6	180.9	3.2	780	474	0.608
4	0.20038	2.80	0.0295	1.37	0.49095	185.4	4.8	187.7	2.5	365	242	0.663
5	0.19525	2.42	0.0290	1.57	0.65095	181.1	4.0	184.3	2.9	854	508	0.595
6	0.21117	2.69	0.0298	1.39	0.51634	194.5	4.8	189.0	2.6	435	273	0.627
7	0.20840	2.02	0.0303	1.37	0.67923	192.2	3.5	192.6	2.6	1137	1440	1.267

Table 2. *Cont.*

Point Number	Isotope Ratio after ^{204}Pb Correction					Isotopic Age (Ma)				Content		
	^{207}Pb/^{235}U	±σ	^{206}Pb/^{238}U	±σ	ρ	^{207}Pb/^{235}U	±σ	^{206}Pb/^{238}U	±σ	U	Th	Th/U
8	0.20686	1.99	0.0305	1.38	0.69345	190.9	3.5	193.9	2.6	2285	2044	0.895
9	0.20464	1.74	0.0302	1.20	0.69176	189.0	3.0	192.0	2.3	1519	1333	0.878
10	0.21327	1.89	0.0308	1.34	0.70914	196.3	3.4	195.9	2.6	1407	908	0.646
11	0.20083	2.55	0.0291	1.26	0.49660	185.8	4.3	184.9	2.3	1577	1369	0.868
12	0.20449	2.91	0.0290	1.50	0.51773	188.9	5.0	184.1	2.7	473	339	0.717
LGC07 Gabbro												
1	0.20620	2.02	0.0296	1.08	0.53535	190.4	3.5	188.2	2.0	1023	573	0.560
2	0.19613	3.03	0.0293	1.12	0.36847	181.8	5.1	186.3	2.0	787	439	0.557
3	0.20391	2.53	0.0293	1.11	0.43743	188.4	4.4	185.9	2.0	841	542	0.645
4	0.21005	3.28	0.0293	1.40	0.42681	193.6	5.8	185.9	2.6	328	231	0.704
5	0.21322	3.26	0.0307	1.09	0.33402	196.3	5.8	194.8	2.1	887	718	0.810
6	0.20551	1.48	0.0295	0.89	0.60235	189.8	2.6	187.5	1.6	2093	3049	1.457
7	0.20634	2.69	0.0300	1.45	0.53677	190.5	4.7	190.4	2.7	573	462	0.807
8	0.19639	3.16	0.0296	1.26	0.39824	182.1	5.3	188.3	2.3	922	792	0.858
9	0.21462	4.00	0.0294	1.49	0.37305	197.4	7.2	186.5	2.7	367	163	0.444
10	0.20589	2.72	0.0296	1.05	0.38604	190.1	4.7	187.8	1.9	783	509	0.651
11	0.20550	2.23	0.0293	0.99	0.44147	189.8	3.9	186.0	1.8	961	583	0.607
12	0.19432	2.83	0.0293	1.07	0.37706	180.3	4.7	186.1	2.0	767	736	0.961
13	0.19932	2.63	0.0292	1.15	0.43827	184.6	4.4	185.6	2.1	937	572	0.611
14	0.20212	2.99	0.0295	1.06	0.35618	186.9	5.1	187.3	2.0	660	332	0.503
15	0.18882	3.59	0.0289	1.06	0.29463	175.6	5.8	184.0	1.9	783	447	0.570
16	0.20743	2.53	0.0296	1.17	0.46209	191.4	4.4	188.2	2.2	591	287	0.485
17	0.19782	3.70	0.0293	1.14	0.30898	183.3	6.2	186.2	2.1	506	368	0.727
18	0.21332	3.57	0.0296	1.38	0.38553	196.3	6.4	187.8	2.6	279	182	0.652
19	0.19916	3.04	0.0287	1.39	0.45738	184.4	5.1	182.7	2.5	431	209	0.483
20	0.21511	3.11	0.0291	1.27	0.41011	197.8	5.6	185.1	2.3	369	174	0.471
21	0.21236	2.57	0.0293	1.12	0.43668	195.5	4.6	186.1	2.1	554	457	0.826
22	0.19393	4.12	0.0292	1.09	0.26461	180.0	6.8	185.4	2.0	626	369	0.589
23	0.20192	3.24	0.0296	1.07	0.33130	186.8	5.5	187.9	2.0	760	467	0.614
Qinghu Standard												
Qinghu1	0.17094	1.56	0.0248	1.14	0.73	160.2	2.3	158.2	1.8	1928	759	0.393
Qinghu2	0.17247	1.84	0.0251	1.45	0.79	161.6	2.8	159.5	2.3	1978	1211	0.612
Qinghu3	0.16661	1.51	0.0249	1.12	0.74	156.5	2.2	158.5	1.8	2161	890	0.412
Qinghu4	0.16941	1.42	0.0251	1.18	0.83	158.9	2.1	159.7	1.9	3476	2083	0.599
Qinghu5	0.17081	1.55	0.0251	1.16	0.75	160.1	2.3	159.8	1.8	2106	980	0.465

Table 3. SIMS zircon O data of gabbro, Laguoco, Tibet.

Point Number	Beam Intensity	Isotope Ratio (Counts)							
		^{16}O	±σ	^{18}O/^{16}O	±σ	^{16}O/^{18}O	±σ	Corrected	1SE
LGC07 Gabbro									
1	2.2	2.485×10^9	0.0352402	0.0020196	0.0092184	495.1505	0.0092168	5.70	0.1843679
2	2.2	2.493×10^9	0.0281669	0.0020217	0.0075936	494.6426	0.0075936	6.74	0.1518719
3	2.2	2.442×10^9	0.0146235	0.0020177	0.0078552	495.6102	0.0078548	4.77	0.1571033
4	2.2	2.475×10^9	0.0331004	0.0020198	0.0061323	495.1059	0.0061315	5.797	0.1226467
5	2.2	2.48×10^9	0.0163116	0.0020185	0.0074009	495.4174	0.0074003	5.167	0.1480181
6	2.2	2.457×10^9	0.0245449	0.0020192	0.0058637	495.2437	0.0058639	5.517	0.1172736
7	2.2	2.608×10^9	0.0362296	0.0020156	0.0068526	496.1309	0.0068542	3.717	0.1370525
8	2.2	2.484×10^9	0.0251973	0.0020181	0.0064952	495.5062	0.0064946	4.98	0.1299048
9	2.2	1.925×10^9	0.02263	0.002014	0.0101105	496.5342	0.0101114	5.38	0.2022094
10	2.2	2.547×10^9	0.0064081	0.002018	0.0113456	495.547	0.0113466	4.89	0.2269126
11	2.2	2.416×10^9	0.0129122	0.0020187	0.0094073	495.3579	0.0094076	5.28	0.188146

Table 3. *Cont.*

Point Number	Beam Intensity	Isotope Ratio (Counts)							
		^{16}O	±σ	$^{18}O/^{16}O$	±σ	$^{16}O/^{18}O$	±σ	Corrected	1SE
12	2.2	2.486×10^9	0.0134447	0.0020183	0.0075554	495.4592	0.0075545	5.07	0.1511072
13	2.2	1.466×10^9	0.3208368	0.0020133	0.0113031	496.7063	0.0113008	2.54	0.2260618
				LGC04 Gabbro					
1	2.1	2.749×10^9	0.0122002	0.0020176	0.0088117	495.6463	0.0088115	5.31	0.1762343
2	2.1	2.759×10^9	0.006298	0.0020175	0.0078579	495.6568	0.0078583	5.29	0.157159
3	2.1	2.759×10^9	0.0118381	0.0020177	0.0072292	495.6169	0.0072297	5.37	0.144584
4	2.1	2.749×10^9	0.0123692	0.0020176	0.0060268	495.6269	0.0060266	5.35	0.120536
5	2.1	2.757×10^9	0.0118871	0.0020177	0.00526	495.606	0.0052604	5.39	0.1052004
6	2.1	2.744×10^9	0.0117654	0.0020176	0.0060675	495.6454	0.0060683	5.31	0.1213492
7	2.1	2.77×10^9	0.0191774	0.0020176	0.0053202	495.6386	0.0053199	5.32	0.1064038
8	2.1	2.767×10^9	0.0147225	0.0020179	0.0047529	495.5593	0.0047529	5.48	0.0950587
9	2.1	2.766×10^9	0.0171804	0.0020179	0.0072458	495.5714	0.0072463	5.46	0.1449155
10	2.1	2.744×10^9	0.0111763	0.0020177	0.0065368	495.6209	0.0065367	5.36	0.1307361
13	2.1	2.758×10^9	0.0084147	0.0020175	0.0053122	495.6599	0.005312	5.28	0.1062436
14	2.1	2.742×10^9	0.0100091	0.0020175	0.0057841	495.6502	0.0063671	5.27	0.115681
15	2.1	2.737×10^9	0.0203797	0.0020173	0.0061142	495.7213	0.0061136	5.16	0.1222841
16	2.1	2.741×10^9	0.012778	0.0020178	0.0098429	495.5856	0.0098446	5.43	0.1968584
17	2.1	2.761×10^9	0.0082263	0.0020178	0.0060097	495.5879	0.0060099	5.43	0.1201948
18	2.1	2.757×10^9	0.0128307	0.0020176	0.0048927	495.6301	0.0048928	5.34	0.0978539
19	2.1	2.787×10^9	0.0331012	0.0020176	0.0061701	495.6363	0.0061695	5.33	0.1234016
20	2.1	2.749×10^9	0.0139685	0.0020176	0.0075401	495.6283	0.0075396	5.34	0.1508019
21	2.1	2.763×10^9	0.0104934	0.0020175	0.0056353	495.6542	0.0056347	5.29	0.112706
22	2.2	2.745×10^9	0.0094053	0.0020176	0.0093334	495.6278	0.0093331	5.35	0.1866681
23	2.1	2.736×10^9	0.0119956	0.0020175	0.0061799	495.6651	0.0061798	5.276	0.1235973
24	2.1	2.725×10^9	0.0059121	0.0020179	0.0054401	495.5714	0.0054396	5.46	0.1088016
25	2.1	2.748×10^9	0.0222021	0.0020175	0.0067419	495.6579	0.0067432	5.28	0.1348376
26	2.1	2.755×10^9	0.0156549	0.0020178	0.0076946	495.5856	0.0076946	5.43	0.1538912
29	2.1	2.749×10^9	0.0057766	0.002018	0.0074054	495.552	0.0074055	5.49	0.1481075
30	2.1	2.75×10^9	0.0097526	0.0020175	0.0058892	495.6586	0.0058898	5.28	0.1177836
31	2.1	2.747×10^9	0.0171469	0.0020175	0.0049891	495.6668	0.004989	5.27	0.0997813

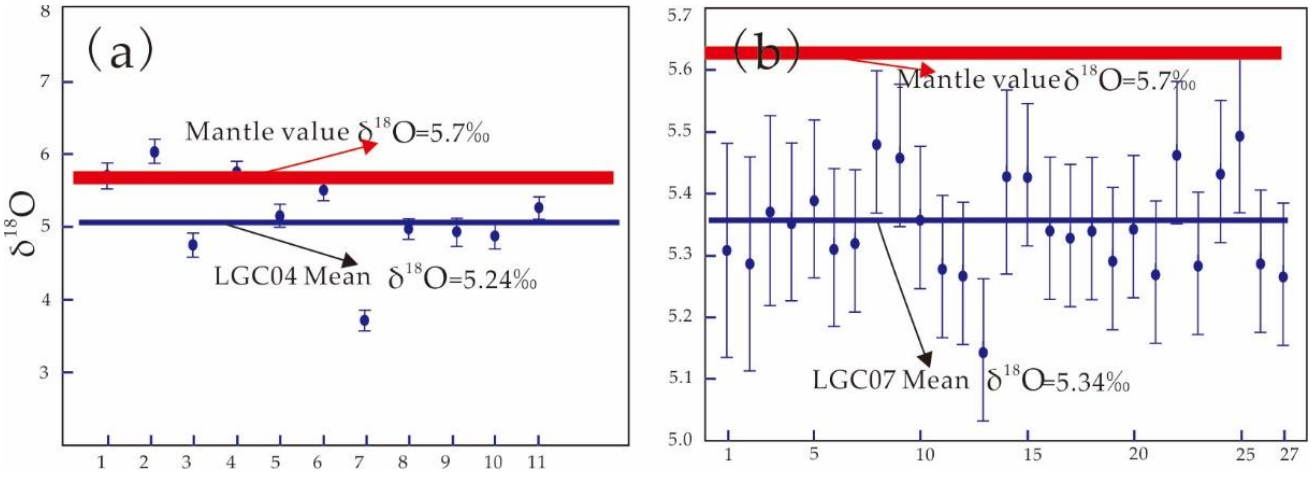

Figure 8. (**a**,**b**) The SIMS oxygen isotope results of gabbro.

5. Discussion

5.1. Petrogenesis

The whole-rock element geochemistry of fundamental rocks can be used to inverse the characteristics of alternative mantle sources. HFSEs (Nb, Ta, Zr, Hf, and Th) and HREEs

can resist late hydrothermal changes [37–40]. The gabbro is abundant in LILEs Rb, Ba, and Sr and depleted in HFSEs Nb, Ta, and Zr (Figure 6b), indicating possible exposure to subduction plate materials during formation.

High Sr/Nd ratios are generally attributed to subducted plate fluids, whereas high Th/Yb ratios are attributed to the addition of subduction sediments [41,42]. Gabbro samples in this study had significantly higher Sr/Nd ratios (139 and 214) than the corresponding values for mid-oceanic ridge basalt (12.33, [33]) and upper crust (11.85, [33]). The gabbro is very depleted in Th, Nb, and Ta (the test content of the sample is lower than the detection limit of the instrument<0.05), with the Th/Yb ratio lower than E-MORB (0.25, [33]). Thus, these HFSE ratios indicate exposure to subduction fluids during formation, whereas subduction sediment melts do not play a significant role. The ratios of the inactive elements Dy/Yb, La/Yb, and Sm/Yb to Sm indicate the compositional characteristics of rock sources [39,40,43]. For the gabbro in Laguoco Tso ophiolite, Dy/Yb-La/Yb (Figure 9a), the relatively high Dy/Yb (1.55 on average) and relatively low La/Yb (0.46 on average) indicate that the source originates from a high degree of partially melted, spinel lherzolite mantle. Sm/Yb-Sm (Figure 9b) shows that the source magma originates from the partial melting of spinel lherzolite, both pointing to a depleted source.

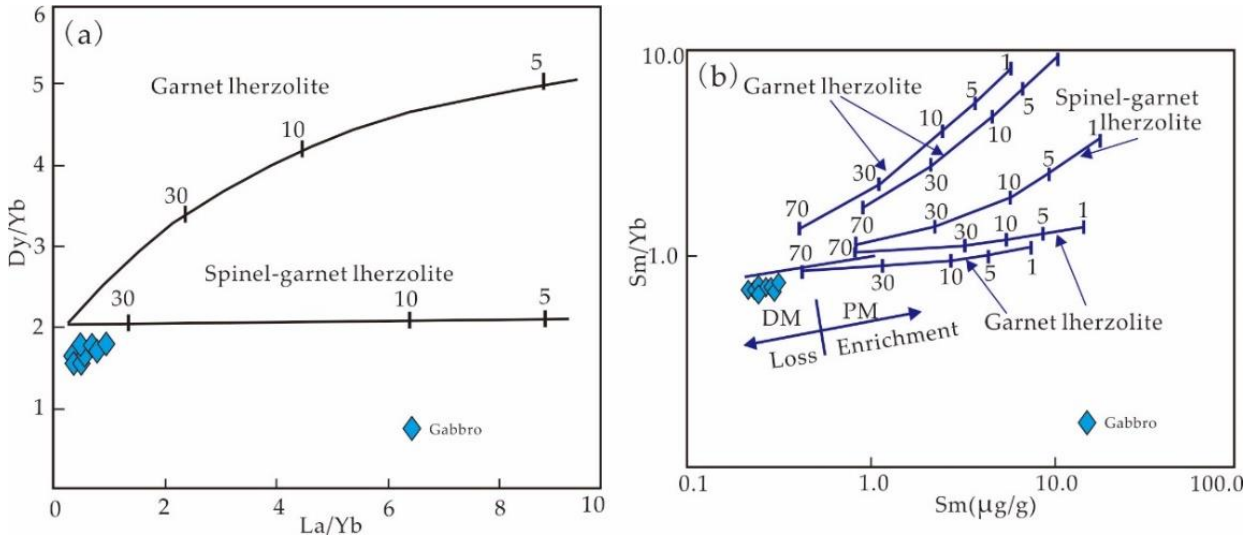

Figure 9. (**a**,**b**) Source characteristics of gabbro rock, Laguoco, Tibet, modified after [39,40].

5.2. Formation Age and Geological Significance

The radiolarian silicalite of the silicalite in the Laguoco Tso ophiolite formed in J_2–K_1 [44], consistent with the zircon age of basic rocks (183–165 Ma) [14] and the zircon age of plagioclase (189–166 Ma) [45,46]. Fundamental rocks commonly had geochemical qualities of an island arc; these ages can denote the subduction time of the oceanic basin. According to the previously published age data for the SLYJZ ophiolite mélange belt (Figure 10), the Kaimeng ophiolite in the east segment formed in the Late Triassic (the zircon age of peridotite is 218 ± 4 Ma [47]); the Nam Co ophiolite in the middle segment formed in the Early Jurassic (the zircon age of gabbro is 178 ± 2.9 Ma [34]; the Rb-Sr age of harzburgite is 166 ± 26 Ma [15]); the Yongzhu ophiolite formed in the Early Jurassic to Early Cretaceous (the zircon age of basic rocks is 178–114 Ma [18,48]; the zircon age of the quartz in the Aso structural mélange belt is 123 Ma [49]).The Laguoco Tso ophiolite in the west segment was formed between the Middle Jurassic and Early Cretaceous (the zircon age of plagiogranite is 189–166 Ma [14,22]; the zircon age of the gabbro is 183.5 ± 2.2 Ma [45]; the diabase's zircon age is 165 ± 3.5 Ma [46]; the Ar-Ar age of amphibolite is 150–137 Ma [46]); the Guchang ophiolite formed in the Early Cretaceous (the age of amphiboles in the gabbro is 128 ± 2.6 Ma [50]); and the Shiquanhe ophiolite formed in the Middle Jurassic (the

zircon age of granitoids is 166–159 Ma [17,19]). Therefore, previous age investigations have confirmed that the age of ophiolites in this suture zone differs across various locations. Additionally, a mature oceanic basin in this ophiolite mélange belt has received extensive subduction processes since the Late Triassic oceanic basin had evolved until the Early Cretaceous.

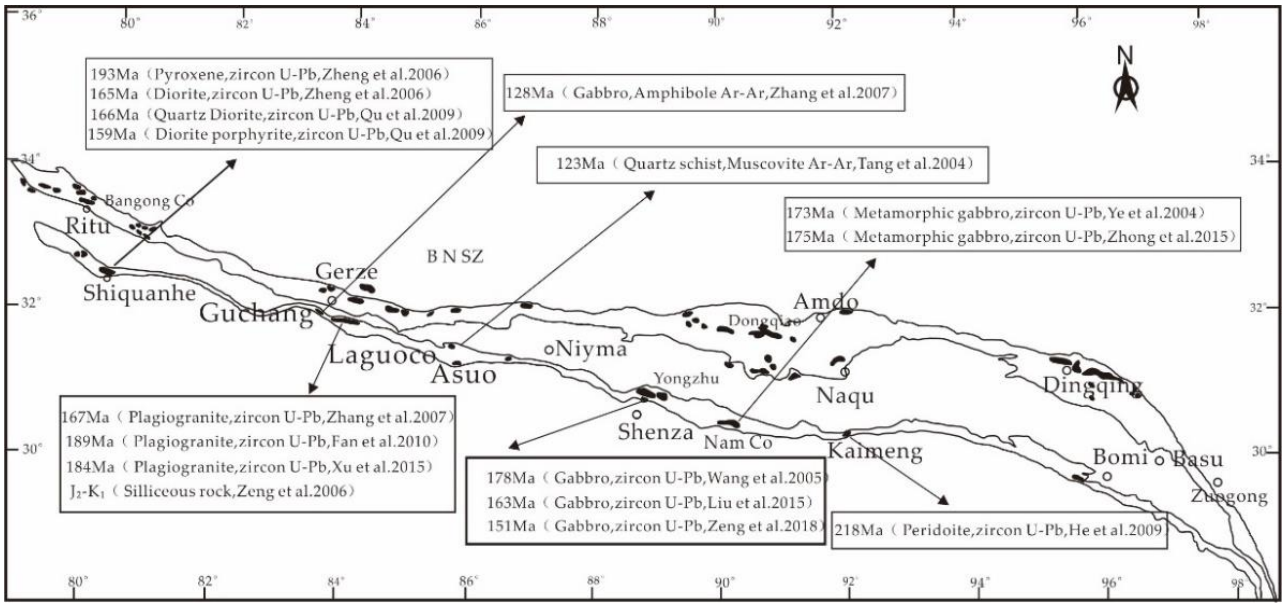

Figure 10. The age distribution of the main ophiolite, the base map modified after [51].

As previously mentioned, the Concordia ages of gabbro samples LGC04 and LGC07 from the Laguoco Tso ophiolite are 189 ± 2.1 Ma and 187 ± 1.2 Ma, respectively. The U and Th content for the two groups of samples is ~117–679 × 10^{-6}, and the U/Th ratio is 0.60–1.4. Given that all the internal structural characteristics in the zircon CL photographs propose that the gabbro zircons are of a magmatic origin with weighted average zircon $\delta^{18}O$ of 5.24‰ ± 0.2‰ and 5.34‰ ± 0.2‰, agreeing with the mantle-derived zircon O isotopes ($\delta^{18}O$ mantle-derived = 5.2‰ ± 0.3‰), it was proposed that zircons of these samples originate from mantle-derived crystallization. This age denotes the crystallization age of gabbro and the formation age of the Laguoco Tso ophiolite.

The SIMS high-accuracy zircon age yielded for the fundamental rocks falls within the 192–189 Ma interval, representing the formation time of the oceanic basin represented by the ophiolite, further providing that the Laguoco Tso ophiolite formed in the Early Jurassic. This understanding establishes that interoceanic subduction occurred in the Neo Tethys oceanic basin in the west segment of the SLYJZ ophiolite mélange belt during the Early Jurassic.

5.3. Tectonic Background

The vast majority of ophiolites in suture zones are SSZ types, which are commonly discovered in forearc basins, back arc basins, island arcs, or small oceanic basins worldwide [3]. Investigations on gabbro in various regions of the SLYJZ ophiolite mélange belt have shown that: for the ophiolite mélange in the western segment, the Shiquanhe ophiolite has the geochemical qualities of MORB, IAT,(the island arc tholelite) and OIB(the ocean island balsalt), and it is an SSZ-type ophiolite [7,10,19,51,52]; the Guchang ophiolite has the geochemical qualities of the MORB, and it was produced in a confined small oceanic basin [49,53]; the Laguoco Tso ophiolite has the geochemical qualities of MORB and IAT and it formed in a basin, inter arc basin or island arc associated with an SSZ subduction environment [14,21,22,46]. For the ophiolite in the middle segment, the Asuo–Yongzhu–Nam Co ophiolite has the geochemical properties of MORB and IAT transition and it was

produced in a back arc or inter arc basin [15,18,48,54]; the Kaimeng ophiolite in the east has the geochemical qualities of IAT and MORB [47].

The gabbro samples from the Laguoco Tso ophiolite in the research area lacked LREEs. They have a chondrite-normalized dispersion pattern similar to E-MORB (Figure 6a). However, compared to E-MORB, their overall REE and trace element levels are lower, indicating a depleted mantle source. Owing to their extreme depletion in the HFSEs, such as U, Th, Nb, and Ta, they have extremely low Th/Yb and reasonably high Zr/Nb. The gabbro samples' TiO_2 contents are quite close (0.16 and 0.17 on average) and are substantially lower than the average value for mid-oceanic ridge basalt (0.8% [41]). In the primitive mantle-normalized trace element pattern (Figure 6b), Sr appears to be positively anomalous, and Zr appears to be negatively anomalous. The V-Ti/1000 and Ti/V-Ti/Sc diagrams (Figure 11a,b) fall in the forearc environment for the Izu–Bonin–Mariana (IBM) boninite; however, they do not have a U-shaped chondrite-normalized REE pattern typical of a boninite. Additionally, for the gabbro samples from the Laguoco Tso basic rocks, the SiO_2 contents are 49.57% and 51.06%, distinct from the recommended value for boninite (SiO_2 > 53% [55]), exempting the feasibility of a boninite. Thus, the samples in this research formed somewhere like an island arc or forearc environment instead of being a boninite. The geochemical evolution of the gabbro is the same as the magmatic evolution in an interoceanic arc environment assumed by prior investigations. It is different from a typical mature back arc basin environment. However, it resembles an inter arc basin environment [56].

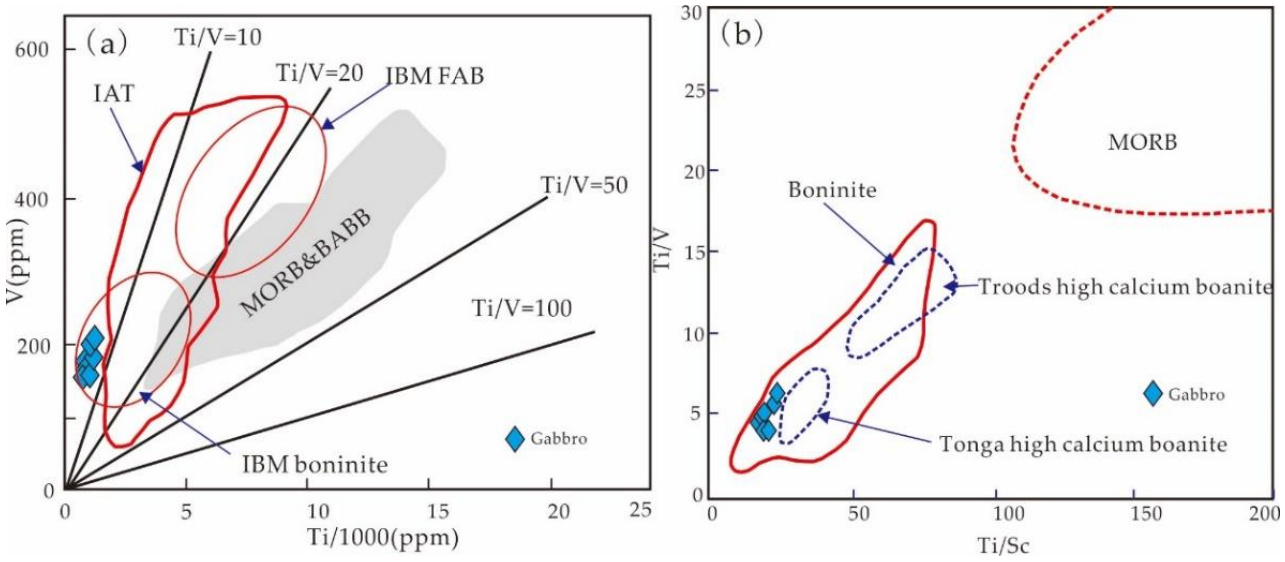

Figure 11. (**a**,**b**) Discrimination diagrams of gabbro tectonic environment, Laguoco, Tibet, modified after [57].

6. Conclusions

(1) The gabbro in the Laguoco Tso ophiolites exhibits the geochemical characteristics of island arc tholeiite (IAT). It is slightly abundant with LILEs (Rb and Ba) and extremely depleted in HFSEs (Nb, Zr, and Ba), suggesting that it was affected by subduction fluids during formation and that it is an SSZ type ophiolite.

(2) A tectonic environment study of gabbro in the Laguoco Tso ophiolite shows either an island arc environment associated with interoceanic subduction or an immature forearc basin environment. The main rock in the parent magmatic source is spinel lherzolite, partially melted to a relatively high degree.

(3) The SIMS zircon U-Pb isotope ages of the gabbro samples from the Laguoco Tso ophiolite are 189 ± 2.1 Ma and 187 ± 1.2 Ma; the O isotopes are 5.24‰ ± 0.2‰ and 5.34‰ ± 0.2‰, indicating feasible interoceanic subduction in this SLYJZ ophiolite mélange belt during the Early Jurassic.

Author Contributions: Y.W. contributed to write the manuscript and the sample analysis; D.-F.G., F.L., M.-K.Q., D.-F.G., J.-S.Y., G.-L.G. and W.-W.W. contributed to the conception of the study and wrote the manuscript; C.Z. performed fieldwork and data analysis. All authors have read and agreed to the published version of the manuscript.

Funding: This work was financially supported by the China Nuclear Geological Survey (DHTLM2101; CHTLM21-08), National Natural Science Foundation of China (Grant No.92062215; 41720104009), and China Geological Survey (DD20221630).

Data Availability Statement: Not applicable.

Acknowledgments: The authors acknowledge Sheng He for the SIMS test. Finally, the authors are grateful to the anonymous reviewers for improving this paper.

Conflicts of Interest: The authors declare no conflict of interest.

References

1. Yin, A.; Harrison, T.M. Geologic evolution of the Himalayan-Tibetan orogen. *Annu. Rev. Earth Planet. Sci.* **2000**, *28*, 211–280. [CrossRef]
2. Moores, E.M. A personal History of the ophiolite concept. *Soc. Am. Spec. Pap.* **2003**, *373*, 17–29.
3. Dilek, Y.; Furnes, H. Ophiolite and their origins. *Elements* **2014**, *10*, 93–100. [CrossRef]
4. Yang, J.S.; Xu, X.Z.; Rong, H.; Niu, X.L. Deep Minerals in Ophiolite Mantle Peridotites: Discovery and Progress. *Bull. Mineral. Petrol. Geochem.* **2013**, *32*, 159–170.
5. Lian, D.Y.; Yang, J.S.; Liu, F.; Wu, W.W. Diamond Classification, Compositional Characteristics, and Research Progress: A Review. *Earth Sci.* **2019**, *44*, 3409–3453.
6. Liu, F.; Yang, J.S.; Lian, D.Y.; Li, G.L. Geological of Neothyan ophiolite in Tibetan Plateau and its tectonic evolution. *Acta Petrol. Sin.* **2020**, *36*, 2913–2945.
7. Hu, C.Z. Characteristics of Shiquanhe-Guchang Ophiolite Belt and its Geologic Significance. *J. Chengdu Coll. Geol.* **1990**, *17*, 23–30.
8. Wang, B.D.; Liu, H.; Wang, L.Q.; He, J.; Wang, D.; Li, F.Q. Spatial-Temporal framework of Shiquanhe-laguoco-Yongzhu-Jiali ophiolite mélange zone, Qinghai-Tibet plateau and its tectonic evolution. *Earth Sci.* **2020**, *45*, 2764–2784.
9. Pang, G.T.; Mo, X.X.; Hou, Z.Q.; Zhu, D.C.; Wang, B.D.; Li, G.M.; Zhao, Z.D.; Geng, Q.R. Spatial-temporal framework of the Gangdese Orogenic Belt and its evolution. *Acta Petrol. Sin.* **2006**, *22*, 521–533. (In Chinese)
10. Zheng, Y.Y.; Xu, R.K.; He, L.X.; Gong, Q.S. The Shiquan River ophiolite mélange zone in Xizang: The delineation and signification of a new archipelagic arc-basin system. *Sediment. Geol. Tethyan Geol.* **2004**, *24*, 13–20. (In Chinese)
11. Baxter, A.T.; Aitchison, J.C.; Zyabrev, S.V. Radiolarian age constraints on Mesotethyan ocean evolution, and their implications for development of the Bangong-Nujiang suture, Tibet. *J. Geol. Soc.* **2009**, *166*, 689–694. [CrossRef]
12. Wu, Z.H.; Ye, P.S.; Hu, D.G.; Liu, Q.S. Thrust System of the North Lhasa Block. *Geol. Rev.* **2003**, *22*, 74–81. (In Chinese)
13. Kapp, P.; Yin, A.; Manning, C.E.; Harrison, M.T.; Taylor, M.H.; Ding, L. Tectonic evolution of the early Mesozoic blueschist-bearing Qiangtang metamorphic belt, Central Tibet. *Tectonics* **2003**, *22*, 1043–1070. [CrossRef]
14. Zhang, Y.X. Tectonic Evolution of the Middle-Western Bangong-Nujiang Suture. Ph.D. Thesis, Guangzhou Institute of Geochemistry, Chinese Academy of Sciences, Beijing, China, 2007. (Unpublished work) (In Chinese).
15. Ye, P.S.; Wu, Z.H.; Hu, D.G.; Jiang, W.; Liu, Q.S.; Yang, X.D. Geochemical chracteristics and tectonic settings of ophiolite of Dongqiao, Tibet. *Geoscience* **2004**, *18*, 309–315. (In Chinese)
16. Geng, Q.R.; Pan, G.T.; Wang, L.Q.; Peng, Z.M.; Zhang, Z. Tetthy evolution and metallogenic background of the Bangong Co-Nujiang belt and the Qiangtang massif in Tibet. *Geol. Bull. China* **2011**, *8*, 1261–1274. (In Chinese)
17. Zheng, Y.Y.; Xu, R.K.; Ma, G.T.; Gao, S.B.; Zhang, G.Y.; Ma, X.M. Ages of generation and subduction of Shiquan river ophiolite: Restriction from SHRIMP zircon dating. *Acta Petrol. Sin.* **2006**, *22*, 895–904. (In Chinese)
18. Zeng, Y.C.; Xu, J.F.; Chen, J.L.; Wang, B.D.; Kang, Z.Q.; Huang, F. Geochronological and geochemical constraints on the origin of the Yunzhug ophiolite in the Shiquanhe-Yunzhug-Namu Tso ophiolite belt, Lhasa Terrane, Tibetan Plateau. *Lithos* **2018**, *300*, 250–260. [CrossRef]
19. Qu, X.X.; Xin, H.B.; Zhao, Y.Y. Opening time of the Bangong Lake Middle Tethys Ocenic basin of the Tibet Plateau: Constrints from Petro-Geochemistry and Zircon U-Pb LA-ICP-MS Dating of Mafic Ophiolite. *Earth Sci. Front.* **2010**, *17*, 53–63.
20. Fan, S.Q.; Shi, R.D.; Ding, L.; Liu, D.L.; Huang, Q.S.; Wang, B.D. Geochemical characteristics and zircon U-Pb age of the plagiogranite in Gaize ophiolite of central Tibet and their tectonic significance. *Acta Petrol. Mineral.* **2010**, *29*, 467–478.
21. Kang, Z.Q.; Xu, J.F.; Wang, B.D.; Cheng, J.L. Qushenla Formation volcanic rocks in north Lhasa block: Products of Bangong Co-Nujiang Tethys's southward subduction. *Acta Petrol. Sin.* **2010**, *26*, 3106–3116.
22. Wang, B.D.; Xu, J.F.; Zeng, Q.G.; Kan, Z.Q.; Cheng, K.L.; Don, Y.H. Geochemistry and genesis of Lhaguo Tso ophiolite in south of Gerze area, Center Tibet. *Acta Petrol. Sin.* **2007**, *23*, 1521–1530.
23. Fan, J.J.; Li, C.; Wang, M.; Xe, C.M.; Peng, T.P.; Liu, H.Y. Material composition, age and significance of the Dong Co Mélange in the Bangong-Nujiang suture zone. *Geol. Bull. China* **2018**, *37*, 1417–1427.

24. Chen, L.; Zhao, Z.F.; Zhong, Y.F. Origin of andesitic rocks: Geochemical constraints from Mesozoic volcanics in the Luzhong basin, South China. *Lithos* **2014**, *190*, 220–239. [CrossRef]
25. Qi, L.; Conrad, G. Determination of trace elements in twenty-six Chinese geochemistry reference materials by Inductively Coupled Plasma—Mass Spectrometry. *Geostand. Newsl.* **2000**, *24*, 51–63. [CrossRef]
26. Slama, J.; Kosler, J.; Condon, D.; Crowley, J.; Gerdes, A.; Hanchar, J.; Horstwood, M.; Morris, G.; Nasdala, L.; Norberg, N.; et al. Plésovice zircon—A new natural reference material for U-Pb and Hf isotopic microanalysis. *Chem. Geol.* **2008**, *249*, 1–35. [CrossRef]
27. Li, X.H.; Tang, G.Q.; Gong, B.; Yang, Y.H.; Hou, K.J.; Hu, Z.C.; Li, Q.L.; Liu, Y.; Li, W.X. Qinghu zircon: A working reference for microbeam analysis of U-Pb age and Hf and O isotopes. *Chin. Sci. Bull.* **2013**, *58*, 4647–4654. [CrossRef]
28. Li, X.H.; Long, W.G.; Li, Q.L. Penglai Zircon Metacysts: A Potential New Working Reference Material for Microbeam Determination of Hf-O Isotopes and U-Pb Age. *Geostand. Geoanal. Res.* **2010**, *34*, 117–134. [CrossRef]
29. Ludwig, K.R. Isoplot/Ex, A Geochronological Toolkit of Granitoids. *J. Geol. Soc. Am. Bull.* **2003**, *101*, 635–643.
30. Middlemost, E.A.K. Naming materials in the magama/igneous rock system. *Earth-Sci. Rev.* **1994**, *37*, 215–224. [CrossRef]
31. Le Maitre, R.W. *Igneous Rocks: A Classification and Glossary of Terms*, 2nd ed.; Cambridge University Press: Cambridge, UK, 2002.
32. Lai, S.C.; Liu, C.Y. Geochemistry and genesis of the island-arc in Anduo area, Tibetan plateau. *Acta Petrol. Sin.* **2003**, *19*, 675–682.
33. Sun, S.S.; McDonough, W.F. Chemical and isotopic systematics of oceanic basalt: Implication for mantle composition and processes. *Geol. Soc. Lond. Spec. Publ.* **1989**, *42*, 528–548. [CrossRef]
34. Hoskin, P.W.; Black, L.P. Metamorphic zircon formation by solid-state recrystallization of protolith igneous zircon. *J. Metamorph. Geol.* **2000**, *18*, 423–439. [CrossRef]
35. Corfu, F.; Hanchar, J.; Hoskin, P.; Kinny, P. Atlas of zircon textures. *Rev. Mineral. Geochem.* **2003**, *53*, 469–500. [CrossRef]
36. Grimes, C.B.; Ushikubo, T.; Kozdon, R.; Valley, J.W. Perspectives on the origin of plagiogranite in ophiolites from oxygen isotopes in zircon. *Lithos* **2013**, *179*, 48–66. [CrossRef]
37. Vally, J.W.; Lackey, J.S.; Cavosie, A.J.; Clechenko, C.C.; Spicuzza, M.J.; Basei, M.A.S.; Bindeman, I.N.; Ferreira, V.P.; Sial, A.N.; King, E.M. 4.4 billion years of crustal maturation: Oxygen isotope ratios of magamatic zircon. *Contrib. Mineral. Petrol.* **2005**, *150*, 561–580. [CrossRef]
38. Pearce, J.A.; Stern, R.J. Origin of back-arc basin magmas: Trace element and isotope perspectives. In *Back-Arc Spreading Systems: Geological, Biological, Chemical, and Physical Interactions*; Christie, D.M., Fisher, C.R., Lee, S.M., Givens, S., Eds.; American Geophysical Union: Washington, DC, USA, 2006; pp. 63–86.
39. Xu, Y.G.; Martin, M.; Thirwall, M.F.; Xie, G. Exotic lithosphere mantle beneath the western Yangtze craton: Petrogenetic links to Tibet using highly magnesian ultra-potassic rocks. *Geology* **2001**, *29*, 863. [CrossRef]
40. Aldanmaz, E.; Pearce, J.A.; Thirlwall, M.F.; Mitchell, J.G. Petrogenetic evolution of late Cenozoic, post-collision volcanism in western anatolia, turkey. *J. Volcanol. Geotherm. Res.* **2000**, *102*, 67–95. [CrossRef]
41. Pearce, J.A.; Stern, R.J.; Bloomer, S.H.; Fryer, P. Geochemical mapping of the Mariana arc-basin system: Implication for the nature and distribution of subduction components. *Geochem. Geophys. Geosyst.* **2005**, *6*, 7. [CrossRef]
42. Pearce, J.A. Geochemical fingerprinting of oceanic basalts with application to ophiolite classification and the search for Archean oceanic crust. *Lithos* **2008**, *100*, 14–48. [CrossRef]
43. Rudnick, R.L.; Gao, S. Composition of the continental crust. Treatise on Geochemistry. In *The Crust*; Elsevier: Amsterdam, The Netherlands, 2003; Volume 3, pp. 1–64.
44. Zeng, Q.G.; Mao, G.Z.; Wang, B.D. *1:250000 Gaize Country and Other 4 Regional Geological Survey Reports*; Geological Publishing House: Beijing, China, 2010. (In Chinese)
45. Xu, J.X. Structural Properties of the Laguoco Ophiolite in Gaize Country, Tibet. Master's Thesis, Jilin University, Changchun, China, 2015. (In Chinese).
46. Yuan, H.J.; Yin, Z.X.; Liu, W.L.; Hang, Q.T.; Liu, H.F.; Wang, Z.F.; Cai, Z.R.; Xia, B. Tectonic Evolution of the Meso-Tethys in the Western Segment of Bangong-Nujiang Suture Zone: Insights from Geochemistry and Geochronology of the Lagkor Tso Ophiolite. *Acta Geol. Sin.* **2015**, *89*, 369–388. (In Chinese)
47. He, Z.H.; Yang, D.P.; Wang, T.W. Age, geochemistry and its tectonic significance of Kaimeng ophiolites in Jiali fault belt, Tibet. *Acta Petrol. Sin.* **2006**, *22*, 588–597. (In Chinese)
48. Wang, Y.S.; Qu, Y.G.; Wang, Z.H.; Zheng, C.Z.; Xie, Y.H.; Sun, Z.G.; Zhang, N.K. Discovery of the Yunzhug sheeted dike swarm in northern Tibet, China-Evidence foe seafloor spreading. *Geol. Bull. China* **2005**, *24*, 1150–1156. (In Chinese)
49. Tang, F.L.; Huang, J.C.; Luo, X.C.; Huang, C.G. The Discovery and Significance of the Asuo Structural Mélanges in North Tibet. *J. East China Inst. Technol.* **2004**, *27*, 245–250.
50. Zhang, K.Z.; Chen, Y.L. Plagiogranite in the Goicang ophiolite in Xizang. *Sediment. Geol. Tethyan Geol.* **2007**, *27*, 32–37.
51. Pan, G.T.; Zhu, D.C.; Wang, L.Q.; Liao, Z.L.; Cheng, Q.R.; Jiang, X.S. Bangong Lake-Nu River suture zone-the northern boundary of Gondwanaland: Evidence from geology and geophysics. *Earth Sci. Front.* **2004**, *11*, 371–382. (In Chinese)
52. Qiu, R.Z.; Deng, J.F.; Zhou, S.; Li, T.D.; Xiao, Q.H.; Guo, T.Y.; Cai, Z.H.; Li, G.L.; Huang, G.C.; Meng, X.J. Ophiolite types in western Qinghai-Tibetan Plateau-Evidence from petrology and geochemistry. *Earth Sci. Front.* **2005**, *12*, 277–291.
53. Yang, R.H.; Li, C.; Chi, X.G.; Wang, T.W. The primary study of geochemical characteristics and tectonic setting of ophiolite in Yongzhu-Namuhu, Tibet. *Geoscience* **2003**, *17*, 14–19. (In Chinese)

54. Mo, X.X.; Lu, F.X.; Shen, S.Y.; Zhu, Q.W.; Hou, Z.Q.; Yang, K.H.; Deng, J.F.; Liu, X.M.; He, C.X. *Volcanism and Mineralization of Sanjiang Tethys*; Geological Publishing House: Beijing, China, 1993; pp. 224–233. (In Chinese)
55. Liu, Z.Y.; Jia, H.M.; Huang, W.P.; Wang, C.Y.; Zhao, H.W.; Wang, Y.S. Achievements and prospects of four 1:50000 regional geological survey projects in southwest Bangor country, Tibet. *Geol. Surv. China* **2015**, *2*, 8–12. (In Chinese) [CrossRef]
56. Xiao, Q.H.; Li, T.D.; Pang, G.T.; Lu, S.N.; Ding, X.Z.; Deng, J.F.; Feng, Y.M.; Liu, Y.; Kou, C.H.; Yang, L.L. Petrologic ideas for identification of ocean-continent transition: Recognition of intra-oceanic arc and initial subduction. *Geol. China* **2016**, *43*, 721–737. (In Chinese)
57. Shervais, J.W. Ti-V Plots and the petrogenesis of Modern and ophiolite lavas. *Earth Planet. Sci. Lett.* **1982**, *59*, 101–118. [CrossRef]